

See discussions, stats, and author profiles for this publication at: <https://www.researchgate.net/publication/332991918>

# Density distribution of asteroid 25143 Itokawa based on smooth terrain shape

Article in *Planetary and Space Science* · May 2019

DOI: 10.1016/j.pss.2019.05.002

CITATIONS

22

READS

273

3 authors:



**Masanori Kanamaru**

The University of Tokyo

16 PUBLICATIONS 244 CITATIONS

SEE PROFILE



**Sho Sasaki**

Osaka University

468 PUBLICATIONS 8,294 CITATIONS

SEE PROFILE



**Mark A Wiczorek**

Observatoire de la Côte d'Azur

261 PUBLICATIONS 13,436 CITATIONS

SEE PROFILE

# Density Distribution of Asteroid 25143 Itokawa Based on Smooth Terrain Shape

Masanori Kanamaru<sup>a</sup>, Sho Sasaki<sup>a</sup>, Mark Wieczorek<sup>b</sup>

<sup>a</sup>*Osaka University*

<sup>b</sup>*Observatoire de la Côte d'Azur*

---

## Abstract

The shape and internal structure of an asteroid is a result of its violent collisional history, and Asteroid 25143 Itokawa is an important target for investigating the internal structure and formation processes associated with rubble pile asteroids. The surface of Itokawa contains numerous boulders and is very rough, but 20% of the surface is covered with centimeter-sized gravels that are called "smooth terrain". These flat areas are associated with low areas of the gravitational potential and are considered to be formed by down-slope migration and accumulation of pebbles. We propose a method to constrain the interior density distribution of an asteroid by modeling the gravity field and fitting the smooth terrains to equi-potential surfaces. Density models that are composed of two distinct lobes best explain the data if the "head" and "body" have different densities of 2,450 kg/m<sup>3</sup> and 1,930 kg/m<sup>3</sup>, respectively. Alternatively, the two lobes could have comparable densities if there was a compressed "neck" of higher density between the two. Three layer models that treat the densities of the head, neck and body separately are largely unconstrained. However, when using an independent estimate of the center-of-mass/center-of-figure offset as determined from modeling the YORP spin-up of Itokawa, our models require the density of the head to be larger than the global average.

**Keywords:** Asteroid 25143 Itokawa, gravity field, density distribution, equi-potential surface

---

## 1. Introduction

The interior structure of small solar system bodies tell us about how planetary objects formed and evolved. In spite of many ground-based observations and spacecraft missions, we have much less information about the interiors of asteroids than of their surface properties. The sizes, bulk densities and inferred porosities of asteroids are some of the most fundamental physical properties for investigating their internal structures and formation processes. Larger asteroids generally have more spherical shapes and higher bulk densities than smaller ones (Carry, 2012). Asteroids with sizes of a few hundred km could have experienced temperatures high enough for them to have fully or partially differentiated (Neumann et al., 2013). On the other hand, smaller asteroids tend to have irregular shapes and lower bulk densities. Their shapes and internal structures result from impact events and the disruption of their parent bodies and subsequent re-accumulation processes.

Asteroid 433 Eros is one of the asteroids that was observed in detail, by the Near Earth Asteroid Rendezvous (NEAR) spacecraft mission (Veverka et al., 2000). The bulk density of Eros is estimated to be  $2,670 \pm 30 \text{ kg/m}^3$  by combining a measurement of its mass and volume (Yeomans et al., 2000). According to the gravity measurements derived from the spacecraft tracking data, the first degree and order terms of the gravity spherical harmonic coefficients ( $C_{11}, S_{11}, C_{10}$ ) show that the center-of-mass (COM) is offset from the center-of-figure (COF) by only  $(-9.7, 2.4, 32.6) \text{ m}$  in each of the three principal axis directions (Miller et al., 2002). The COM-COF offset is small for Eros' size of  $34.4 \times 11.2 \times 11.2 \text{ km}$  and it implies that there is no significant hemispherical density contrasts (Miller et al., 2002; Konopliv et al., 2002). Other gravity coefficients up to several degrees and orders are also consistent with a uniform interior density distribution (Miller et al., 2002; Konopliv et al., 2002). Asteroid Eros is commonly classified as a coherent and strength dominated object with interior fractures, whose porosity is estimated to be approximately 20% (Wilkison et al., 2002).

The Near-Earth asteroid 25143 Itokawa was visited by the Japanese spacecraft mission, Hayabusa (Fujiwara et al., 2006). Itokawa is a sub-kilometer sized asteroid (535 meters by 294 meters by 209 meters) with a low bulk density of  $1,950 \pm 140 \text{ kg/m}^3$  and a bi-lobed

29 shape. The distinctive shape of Itokawa is often compared to a shape of a sea otter and its two  
30 lobes are called the "head" and the "body". Based on estimates of its composition and bulk  
31 density, this object is believed to contain a porosity of about 40% (Abe et al., 2006a,b). It is an  
32 important and unique target for better understanding the formation processes of small rubble-  
33 pile asteroids that are common in the asteroid belt. The Hayabusa mission team estimated  
34 the mass of Itokawa from the spacecraft orbit during a descent operation with an uncertainty  
35 of 5% (Abe et al., 2006b), but the gravity field at higher degree and order was not observed.  
36 Thus, based solely on the observed mass measurement, it is difficult to determine whether the  
37 interior density distribution is homogeneous or not.

38 The surface of Itokawa is composed of rough terrain that is comprised of boulders, but  
39 about 20% of the surface is covered with centimeter-sized gravels that are commonly called  
40 "smooth terrain" (Fujiwara et al., 2006; Saito et al., 2006; Demura et al., 2006). This smooth  
41 terrain is associated with areas where the gravitational potential is low, and is considered  
42 to have formed by the downslope mass movement and accumulation of the fine gravels  
43 (Miyamoto et al., 2007). Over geologic time, it would be expected that the finest grained  
44 materials would approach the shape of an equi-potential surface (see Richardson and Bowling,  
45 2014), analogous to other strengthless materials such as Earth's oceans.

46 The objective of this study is to develop a method to estimate interior density distribution  
47 within a small solar system body. Our method is based on estimating the gravity field  
48 for the object using a topographic shape model and an *a priori* interior density structure.  
49 We then determine the heights of the surface above an equi-potential surface and vary the  
50 density structure such that the smooth terrains approximate locally equi-potential surfaces.  
51 We applied this estimation method to asteroid Itokawa, aiming to determine if there is a  
52 difference in density between its two lobes, the head and body, or if the adjoining "neck" is  
53 compressed. In Section 2, we describe how we simulate the gravity field of an asteroid with  
54 an arbitrary density distribution. The inversion technique to estimate the density distribution  
55 is then described in Section 3. In Section 4, we present the results of our inversion, and in  
56 Section 5, we discuss the implications our work.

## 2. Gravity modeling of small bodies

The classical way to represent the gravity field of a celestial object is through the spherical harmonic expansion of its gravitational potential. With this approach, the gravitational potential can be expressed at a position of radius  $r$ , latitude  $\theta$  and longitude  $\lambda$  as follows:

$$U(r, \theta, \lambda) = \frac{GM}{r} \left[ 1 + \sum_{l=1}^{\infty} \sum_{m=0}^l \left( \frac{R}{r} \right)^l P_{lm}(\sin \theta) (C_{lm} \cos m\lambda + S_{lm} \sin m\lambda) \right] \quad (1)$$

where  $G$ ,  $M$  and  $R$  are the Newtonian constant of gravitation, the total mass of the body and the reference radius of the spherical harmonic coefficients, respectively.  $P_{lm}$  is the associated Legendre function of degree  $l$  and order  $m$ , and the spherical harmonic coefficients  $C_{lm}$  and  $S_{lm}$  reflect information on the shape and interior density distribution of the body. Using the gravity harmonic coefficients determined by spacecraft dynamics, the gravitational potential can be computed at any arbitrary position exterior to the smallest sphere that encloses the object, the so-called Brillouin sphere. The gravitational harmonic coefficients of an asteroid can be also calculated directly by integrating the density distribution throughout its entire body if the density distribution is known *a priori*. Given a polyhedral shape model of an asteroid, whose surface is covered with triangular facets, it is possible to calculate the spherical harmonic coefficients analytically (Werner, 1997). In some cases, it is possible to constrain the interior density distribution within a small body by a least squares fitting between simulated and measured gravitational coefficients (Scheeres et al., 2002; Takahashi and Scheeres, 2014).

It is known that spherical harmonic expansions can diverge in the vicinity of an irregular shaped asteroid and that they are not always suitable to calculate the gravity field on the surface of an asteroid, particularly when the observational point is below the Brillouin sphere (as an example see Hirt and Kuhn (2017)). Direct integration of a constant-density polyhedron has been widely used to avoid this problem (Werner and Scheeres, 1997). The polyhedral approach is an analytic integration of the mass distribution within a polyhedron, based on the assumption that the density is uniform across the entire object. This method is free from divergence and is capable of calculating the gravity field at any point above or below the surface.

In this study, we adopted a method where the object is decomposed into connecting tetrahedral elements. Instead of calculating the gravitational potential of this polyhedron analytically, to save computational time, we placed a single point mass in the interior of each individual tetrahedron. This "mascon" (short for "mass concentration") method is easy to be implemented for an arbitrary density distribution, and the accuracy can be adjusted by changing the characteristic size of each tetrahedron. This technique is described in the following section.

### 2.1. Mascon gravity modeling

A polyhedral shape model of the asteroid Itokawa was constructed from Hayabusa spacecraft images by means of the stereophotoclinometry (SPC) method by Yoshikawa et al. (2012). The initial shape model contained only surface triangular facets, so the shape model was imported into the Netgen Mesh Generator (Schöberl, 1997), which is a 3D Delaunay triangulation library, and the polyhedral shape model was divided into numerous volume elements. Every volume element has the shape of a tetrahedron, and facets that are exposed on the surface of the polyhedron are recognized as surface elements. We prepared numerical mesh models of Itokawa using four different resolutions, which are characterized by the number of volume and surface elements,  $N_V$  and  $N_S$ , respectively. These four shape models are listed in Table 1 along with the average sizes of the volume and surface elements,  $\bar{D}_V$  and  $\bar{D}_S$ , respectively. The original shape model is made of 786,432 surface facets, which has an average horizontal spatial resolution of about 0.8 meters.

A mascon model expresses the gravitational potential of an object by summing the gravitational potential of a number of point masses. For our approach, we placed a single point mass at the centroid of each tetrahedral volume element. The gravitational potential  $U_{grav}$  can be calculated at an arbitrary location  $\mathbf{r}$  using

$$U_{grav}(\mathbf{r}) = -G \sum_{i=1}^{N_V} \frac{\rho_i v_i}{|\mathbf{r}_i - \mathbf{r}|} \quad (2)$$

where  $\rho_i$ ,  $v_i$  and  $\mathbf{r}_i$  are the density, volume and the vector position of the  $i$ th volume element, respectively. Densities of volume elements will be assigned later according to a model of

Table 1: Shape models of Itokawa using four different resolutions along with the original shape model constructed by Yoshikawa et al. (2012). The shape model resolution is characterized by the number of volume elements and surface elements,  $N_V$  and  $N_S$ , respectively.  $\bar{D}_V$  denotes the mean diameter of a sphere of equivalent volume and  $\bar{D}_S$  denotes the mean diameter of a circle of equivalent area of the surface elements.

	$N_V$	$N_S$	$\bar{D}_V$ [m]	$\bar{D}_S$ [m]
Original	—	786,432	—	0.8
(1)	282,987	60,774	3.2	2.3
(2)	1,083,253	142,252	2.0	1.5
(3)	1,693,335	149,062	2.3	1.5
(4)*	3,613,429	173,974	2.0	1.5

\*Highest resolution model used for the later analysis.

the object's density distribution, under the condition that the total mass is equal to the known mass of the asteroid.

In a reference frame attached to a rotating asteroid, the surface potential is affected by its rotation. After computing the gravitational potential as stated above, we added the correspond rotational potential  $U_{rot}$  to the mascon solution. The sum of the gravitational and rotational potential is given as

$$\begin{aligned}
 U(\mathbf{r}) &= U_{grav} + U_{rot} \\
 &= -G \sum_{i=1}^{N_V} \frac{\rho_i v_i}{|\mathbf{r}_i - \mathbf{r}|} - \frac{1}{2} \omega^2 r_{\perp}^2
 \end{aligned} \tag{3}$$

where  $\omega$  is the spin rate of the Itokawa's rotation, and  $r_{\perp} = \sqrt{x^2 + y^2}$  is the distance perpendicular to the rotation axis. The rotation axis is aligned with the z-axis of the shape model, and the rotation period of Itokawa is 12.1324 hours (Fujiwara et al., 2006). The total gravity vector  $\mathbf{g}$  is obtained by taking the space derivative of Eq. (3).

$$\mathbf{g}(\mathbf{r}) = G \sum_{i=1}^{N_V} \frac{\rho_i v_i}{|\mathbf{r}_i - \mathbf{r}|^3} (\mathbf{r}_i - \mathbf{r}) - \omega^2 \mathbf{r}_{\perp} \tag{4}$$

119 In order to obtain a global map of the gravity field on the surface of the asteroid, it is only  
 120 necessary to evaluate Eqs. (3) and (4) at locations  $\mathbf{r}$ , where  $\mathbf{r}$  is taken as the centroid of every  
 121 surface facet.

122 Given our approximation of treating tetrahedral elements by mascons, there is a risk that  
 123 the point-mass approximation could give rise to a significant error, especially in the vicinity  
 124 of the asteroid's surface. We evaluated the calculation error of the mascon modeling approach  
 125 by comparing it to the polyhedral approach of Werner and Scheeres (1997). The relative error  
 126 of the potential  $\varepsilon_U$  between the two techniques at a position  $\mathbf{r}$  is defined as

$$\varepsilon_U(\mathbf{r}) = \left| \frac{U_{\text{mascon}}(\mathbf{r}) - U_{\text{polyhedron}}(\mathbf{r})}{U_{\text{polyhedron}}(\mathbf{r})} \right| \quad (5)$$

127 and the relative error of the magnitude of the gravitational acceleration,  $\varepsilon_g(\mathbf{r})$  is defined in a  
 128 similar manner.

129 Figure 1 shows the relative error of the potential (a) and acceleration (b) as a function of  
 130 the number of the volume elements  $N_V$  utilized in the 3D shape model. We utilized shape  
 131 models of Itokawa using four different resolutions ( $N_V = 282,987, 1,083,253, 1,693,335$  and  
 132  $3,613,429$ ) as listed in Table 1. In these plots, the central horizontal line of each grey box  
 133 indicates the median of the errors calculated on every surface element of the shape model.  
 134 The upper and lower limits of each box represent the first and third quartile, respectively,  
 135 and the maximum and minimum errors are shown by the extent of the vertical lines. In  
 136 general, the accuracy of the mascon modeling improves as the number of the point masses  
 137 increases. Furthermore, we note that the acceleration relative errors are always larger than the  
 138 potential relative errors because the acceleration of point-masses attenuate by the square of the  
 139 distance and are more influenced by each adjacent volume element. For our nominal model  
 140 used in the later analyses that contains  $N_V = 3,613,429$  volume elements and  $N_S = 173,974$   
 141 surface elements, the median relative errors of the gravitational potential and acceleration  
 142 are  $3.7 \times 10^{-6}$  and  $2.2 \times 10^{-3}$ , respectively. The maximum relative errors are respectively  
 143  $5.7 \times 10^{-5}$  and  $2.2 \times 10^{-2}$ . The tests show that the results presented later are insensitive to  
 144 changing the number of volume elements by an order of magnitude.



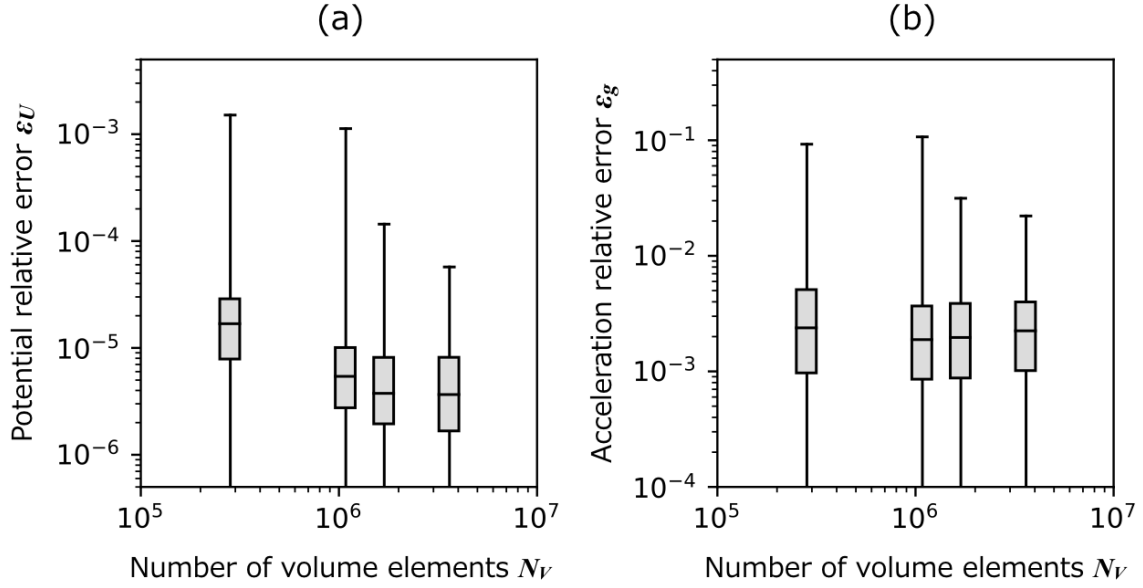


Figure 1: Relative errors of the potential (a) and the magnitude of the acceleration (b) as a function of the number of volume elements of the Itokawa shape model. Relative errors are defined as the difference between a mascon solution, where tetrahedral elements are approximated by point masses, and an analytical solution for the entire polyhedral shape. The central horizontal line represents the median, boxes represent the limits of the first and third quartiles, and the vertical lines denote the maximum and minimum relative errors.

## 145 2.2. Elevation

146 Given a shape model of an asteroid, as well as an estimate of the gravitational potential  
 147 and acceleration on the surface, we can compute the distance of each surface element above  
 148 or below a constant potential surface. This is commonly referred to as the dynamic height,  
 149  $h$ , and can be computed to first order using a Taylor series expansion of the potential with  
 150 respect to an arbitrary reference value

$$U(r + h) = U(r) + \frac{dU(r)}{dr}h \quad (6)$$

151 where  $r$  is the reference radius and where the potential  $U(r)$  is defined to be  $U_{ref}$ . Approx-  
 152 imating the radial derivative of the potential as the gravitational acceleration on the surface  
 153  $g_s$ , this can be rearranged into the familiar form (e.g., Thomas (1993)):

$$h(\mathbf{r}) = \frac{U(\mathbf{r}) - U_{ref}}{g_s(\mathbf{r})} \quad (7)$$

154 For global mapping, the reference potential  $U_{ref}$  will be chosen to be equal to the average  
 155 potential across the surface of the object. However, later, we will also make use of the average  
 156 potential within a specific region. The potential  $U(\mathbf{r})$  is calculated in the center of every  
 157 surface element and average values are computed taking into account the area of each surface  
 158 element. The elevation has a dimension of length and is simply how high or low a certain place  
 159 is above or below the reference potential. Mass wasting processes generally move materials  
 160 downslope, which corresponds to regions of decreasing dynamic elevations.

161 In Figure 2, we show the dynamic elevations that we computed for Itokawa. The global  
 162 map of the dynamic elevations is visualized by Mayavi, 3D scientific data visualization tool  
 163 (Ramachandran and Varoquaux, 2011). Here, we have used a shape model with 3,613,429  
 164 volume elements and 173,974 surface elements, which is the highest resolution model in  
 165 Table 1 and Figure 1, and have assumed a constant density of the body when computing the  
 166 gravitational potentials and accelerations. The mean density of Itokawa is here assumed to be  
 167 2,020 kg/m<sup>3</sup>, derived from the mass measurement by Abe et al. (2006b) and the volume of  
 168 the above shape model. The elevations vary from -25 to 54 meters, and the lowest elevations

are found to be located in MUSES-C Regio, which is a region that is extremely smooth and that lacks large boulders.

The greatest uncertainty in calculating the dynamic heights (for a given mass distribution model) concerns the calculation of the gravitational acceleration at the surface. Our sensitivity tests in Figure 1 show that the average uncertainty is less than 0.3% but that the uncertainty can be as high as 2% in some regions. Given that the largest dynamic elevations are about 54 meters, this suggests that the average uncertainty is about 0.16 meters, and that the maximum error is about 1 meter.

### 3. Density Distribution Estimation

Itokawa has extensive regions that are composed of smooth terrains (Fujiwara et al., 2006). It has been noted previously that these correspond approximately to regions of low gravitational potential, and that mass-wasting processes would have a tendency to move materials downslope into these regions (Miyamoto et al., 2007). In this study, we will make the assumption that these regions correspond to an equi-potential surface, which is the final equilibrium state of surfaces that undergo erosive processes. With the observed shape of the body, we then invert for the density distribution within the asteroid to find those solutions that best provides a flat surface in the regions of the smooth terrains. As a part of this analysis, we mapped the regions of the smooth terrain using both the shape model of Itokawa and visible imagery as described in Section 3.1. In Section 3.2, we describe the inversion technique of the interior density distribution and *a priori* density structures that will be tested in this paper.

#### 3.1. Smooth terrain mapping

We used the Small Body Mapping Tool (SBMT) for mapping the smooth terrain on Itokawa, which is a 3D visualization tool for mapping geological features and is capable of projecting spacecraft images onto shape models (Ernst et al., 2018). A global mosaic map of Itokawa ( $3,600 \times 7,200$  pixels) constructed by Stooke (2012) was projected onto the same shape model used for computing the surface elevations. The shape model used for this purpose contains 173,974 surface elements, and the average of the equivalent circle diameter of

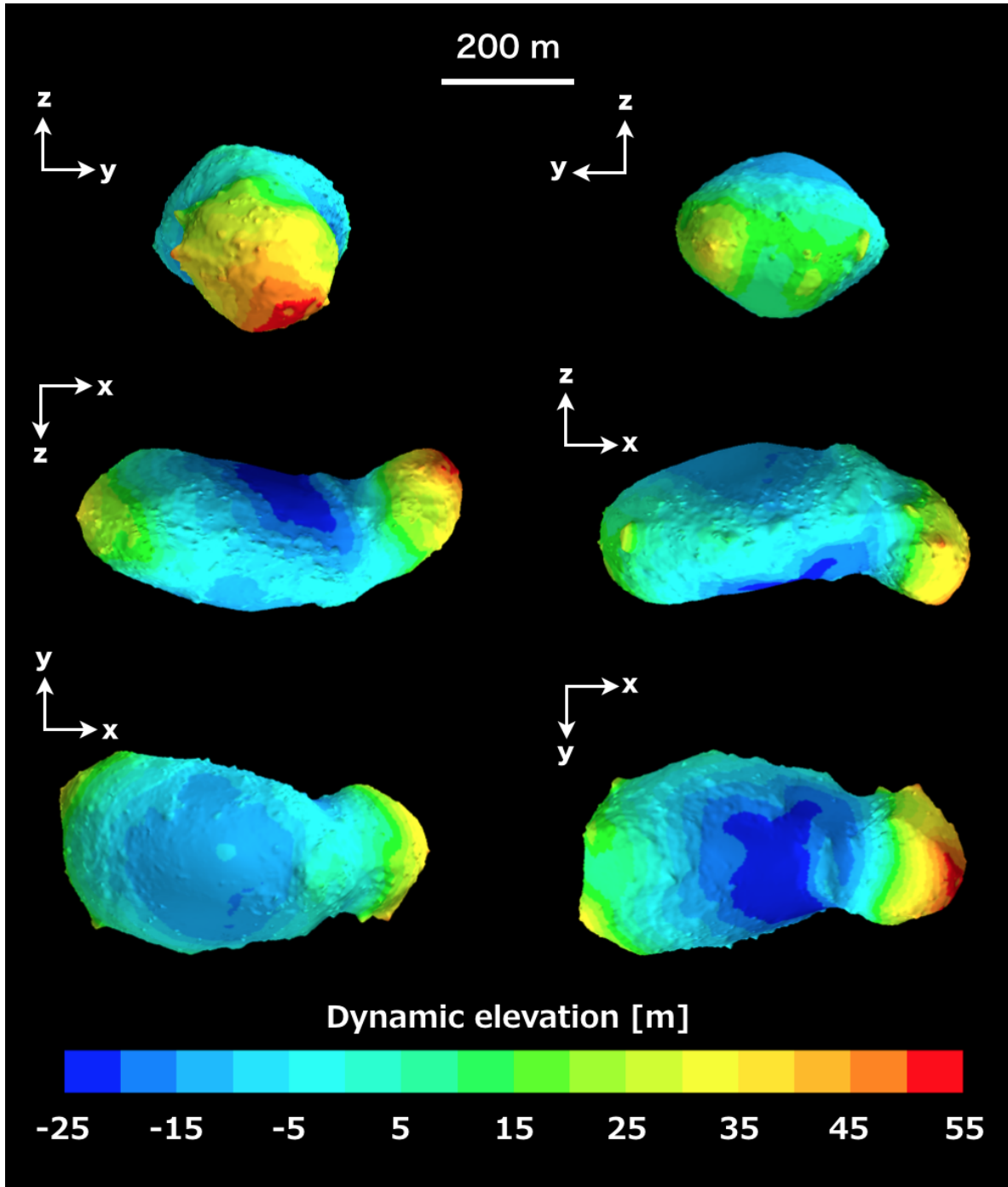


Figure 2: Global map of the dynamic elevations of Itokawa, viewed from  $\pm x$ ,  $\pm y$  and  $\pm z$  axes. Here, we assumed a uniform density throughout the asteroid and defined the average potential across the surface as the reference potential.

each surface element is 1.5 meters. Since the cylindrical projection of the global mosaic was sometimes distorted, we used other visible images that were obtained by the Asteroid Multi-band Imaging CAmera (AMICA) for identifying the smooth terrain (Nakamura et al., 2001; Saito et al., 2006). The best images for mapping the smooth terrains of MUSES-C Regio are ST\_2472657784\_v and ST\_247431509\_v. We chose ST\_2480981469\_v, ST\_2481442195\_v and ST\_2481672682\_v for mapping other smooth terrains in the north polar region, including Sagamihara and Uchinoura Regio. The spatial resolutions of the projected images are approximately 0.4 to 0.5 meters per pixel.

In mapping the extent of smooth terrains on Itokawa, we utilized two criteria. First, we made use of the above images, and drew tentative boundaries around regions that were visibly smooth and had only a small number of obvious boulders. As a secondary criteria for identifying the smooth terrain, we also used the surface roughness derived from the shape model. The roughness parameter at a specific location is here defined as the standard deviation of the surface elevations within a circle of a specific scale (that is, a diameter of the circle). We used the surface roughness in 6 meter diameter circles to help define the boundaries of the smooth terrain. As shown in Figure 3, the surface roughness ranges from less than 0.1 meters to 2.1 meters across the surface of Itokawa, and it highlights the flatness of the smooth terrains with respect to the roughness of the other rocky regions. Finally, we combined the two tentative boundary maps and decided upon a single boundary that best fit both observations.

The mapped smoothed regions included MUSES-C Regio, Sagamihara Regio and Uchinoura Regio as shown in Figure 4. MUSES-C Regio is the largest smooth terrain on Itokawa, and is located in the south polar region. This region was divided into five pieces for ease of use with the SBMT for exporting the geometry of the surface elements (Region ID: 1-a to 1-e). Sagamihara Regio is the second largest smooth terrain on Itokawa in the north polar region (Region ID: 2). There exist many boulders in Sagamihara and its boundary is not as clear and distinct as for MUSES-C Regio. The third largest smooth terrain, Uchinoura is a circular depression with a flat floor that is adjacent to Sagamihara Regio (Region ID: 3) (Hirata et al., 2009). All extracted regions are summarized in Table 2.

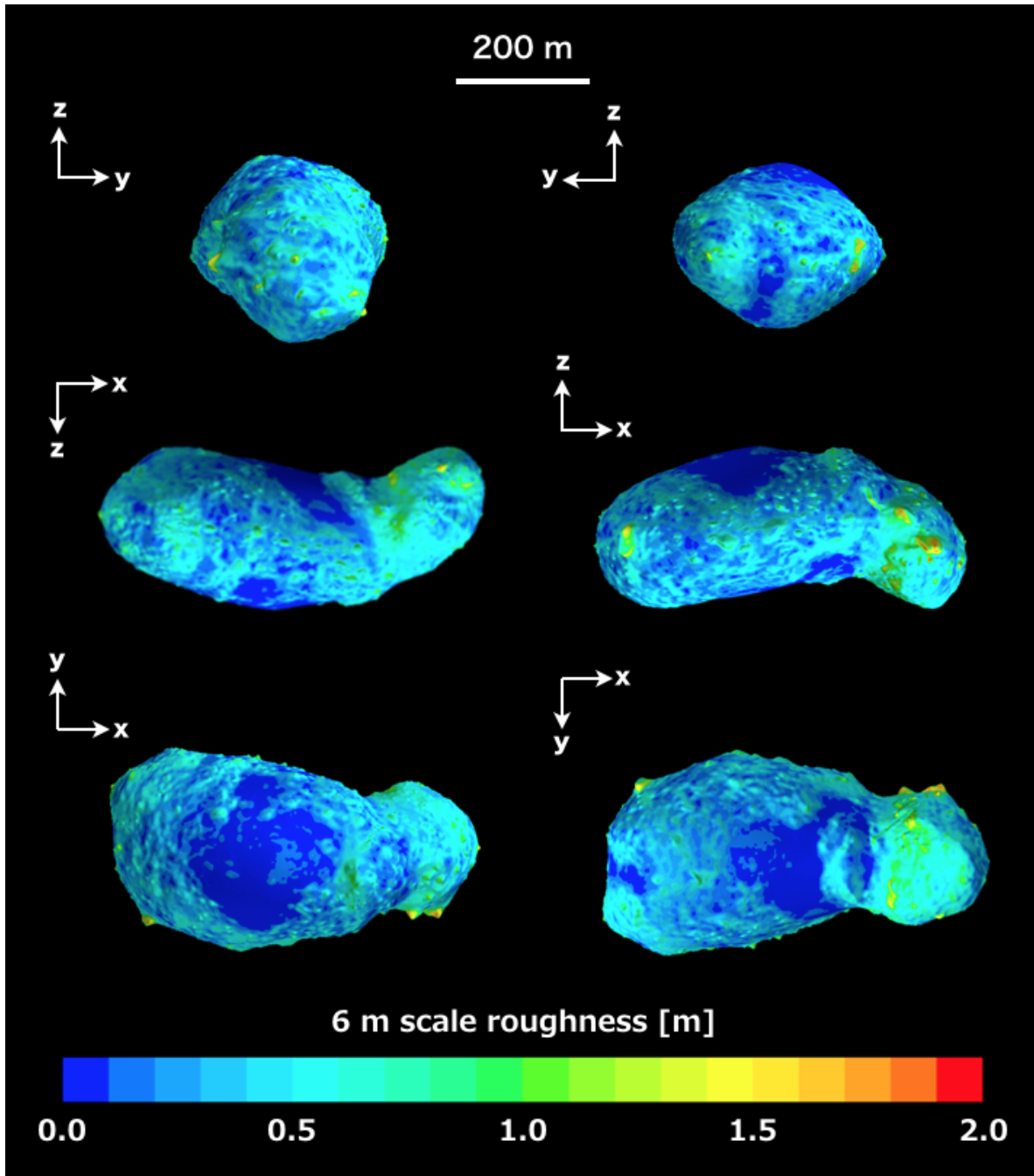


Figure 3: Global map of the surface roughness of Itokawa visualized by Mayavi. The surface roughness is here defined as the standard deviation of the dynamic elevations within a 6 meter diameter circle for every surface element.

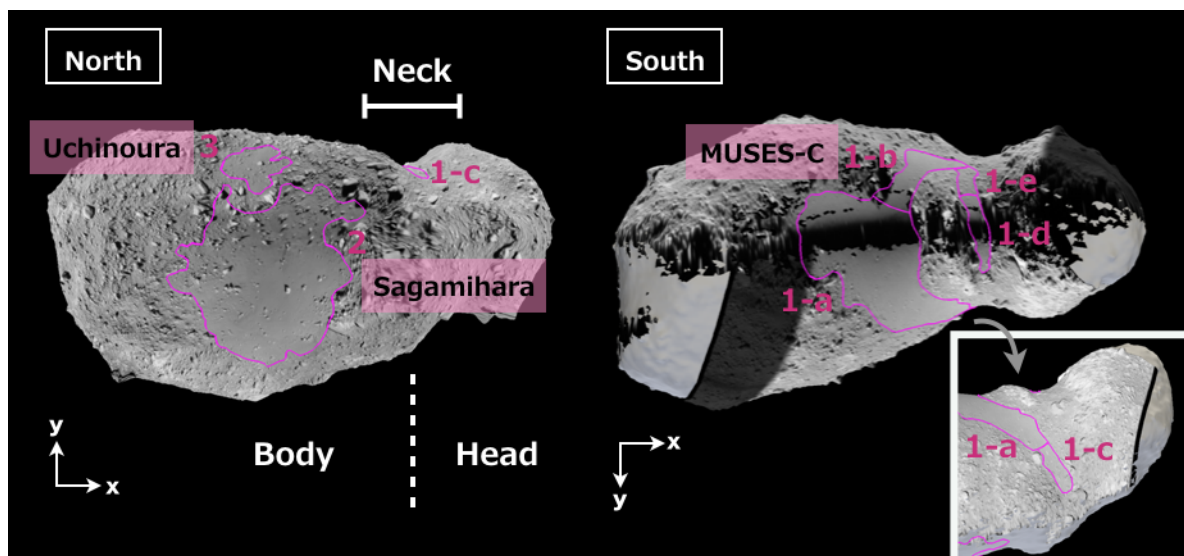


Figure 4: Smooth terrain mapped on Itokawa based on visible imagery and surface roughness. Some images are projected onto the 3D shape model of Itokawa by the Small Body Mapping Tool.

Table 2: Properties of the mapped smooth terrains. The mean elevation in each region is derived from the gravitational potential of a uniform density body according to Eq. (7), and the reference potential of the dynamic elevations is the mean potential over the surface of Itokawa. The surface roughness is defined as the elevation standard deviation within 6 meter diameter circles.

ID number	Location (°N, °E)	Area [m <sup>2</sup> ]	Mean elevation [m]	Mean roughness [m]	Descriptions
1-a	(-57, 56)	17,747	-21.8	0.096	MUSES-C Regio.
1-b	(-32, 321)	3,913	-21.0	0.11	MUSES-C Regio.
1-c	(17, 28)	1,321	-13.8	0.27	MUSES-C Regio.
1-d	(-29, 4)	1,692	-16.6	0.15	A part of MUSES-C in the neck region between the two lobes.
1-e	(-23, 339)	1,088	-18.5	0.12	A part of MUSES-C with a larger concentration of boulders.
2	(67, 225)	24,653	-13.8	0.077	Sagamihara Regio. Numerous boulders exist in this region.
3	(46, 110)	3,261	-12.3	0.075	Uchinoura Regio. A circular depression with a smooth floor.



### 224 3.2. Inversion technique

225 Richardson and Bowling (2014) were the first to investigate a method to estimate the bulk  
226 density of a small body by minimizing the variance of the gravity potential on its surface.  
227 This method assumes that over geologic time, mass-wasting processes will act to redistribute  
228 materials such that the surface will tend toward an equi-potential surface. If there exists loose  
229 regolith on the asteroid, seismic shaking induced by meteorite bombardments would help  
230 to trigger mass movement from high standing regions to low standing regions. The surface  
231 gravity field of an asteroid depends on both the gravitational potential and the rotational  
232 potential, with the former depending upon the assumed density. Though the bulk density can  
233 be estimated by minimizing the difference between the observed shape of the asteroid and an  
234 equi-potential surface, they found that the method did not work well for Itokawa. Applied  
235 globally, they obtained a bulk density of  $330 \text{ kg/m}^3$ , which is far lower than the known value.  
236 When applied to the region of Sagamihara, a more realistic value was obtained, but with large  
237 uncertainties. In any case, their study did not consider the possibility of different densities for  
238 the head, body or neck regions that we consider here.

239 In a different study, Motooka and Kawaguchi (2012) and KANAMARU and SASAKI  
240 (2019) attempted to fit the global shape of Itokawa to a single equi-potential surface. In  
241 contrast to Richardson and Bowling (2014), they investigated how modifying the densities  
242 of the head and body affected the global fit. However, given the two lobe structure of the  
243 asteroid, and the presence of both smooth and rough terrains, it is unlikely that the global  
244 shape would approximate a single equi-potential. In this study, we instead hypothesize that  
245 the smooth terrain is formed by the accumulation of fine gravels and that it is only these  
246 surfaces that should approximate flat surfaces. Under this hypothesis, the remaining regions  
247 have sufficient strength to retain the bi-lobed structure of the asteroid over geologic time.

248 For our inversions that invert for the density distribution in Itokawa, we define the misfit  
249 to be the standard deviation of the dynamic elevations in the smooth terrain with respect to

250 the average dynamic elevation of the unit.

$$\sigma_h = \sqrt{\sum_{i=1}^{n_S} A_i (h_i - h_{mean})^2 / \sum_{i=1}^{n_S} A_i} \quad (8)$$

251 where  $h_i$  and  $A_i$  are the dynamic elevation and area of the  $i$ th surface element in each region  
 252 that is composed of  $n_S$  surface elements. The mean dynamic elevation  $h_{mean}$  is the weighted  
 253 average of the smooth terrain elevations by the areas of each surface element.

$$h_{mean} = \sum_{i=1}^{n_S} A_i h_i / \sum_{i=1}^{n_S} A_i \quad (9)$$

254 The best fitting model is the model that possesses the smallest standard deviation  $\sigma_{h,min}$ .

255 Given that we have no constraints on the gravity field of Itokawa (besides its total mass),  
 256 and that the inversion for the internal density structure of a body is inherently non-unique,  
 257 we have decided to parameterize the density structure of Itokawa in a simple manner. In  
 258 particular, based on the morphology of the body, we will consider models where the density  
 259 of the two lobes of Itokawa differ, and where the density of the neck region is different from  
 260 the two lobes. For these models, each component will be treated as having a constant density.  
 261 This simplifies our gravity calculations enormously, as we only need to calculate the gravity  
 262 field of each component a single time using a density of 1.0: the gravity for an arbitrary  
 263 density is then obtained by multiplying the obtained values by the actual density.

264 For our inversions, we assumed three types of density maps as demonstrated in Figure 5.

- 265 • The compressed head model: In this model, the head and body of Itokawa have different  
 266 densities as shown in the left panel of Figure 5. The boundary of the two lobes is here  
 267 defined at  $x = 150$  m in the body fixed frame, with the center being defined as the  
 268 center-of-figure of the asteroid. By choosing the density of one lobe, the density of the  
 269 other can be obtained using the known total mass.
- 270 • The compressed neck model: In this model, the contact of the two lobes is considered  
 271 to be a finite width neck that has a different density than the head and body. The extent  
 272 of the neck is here defined from  $x = 120$  m to  $x = 180$  m as shown in the right panel

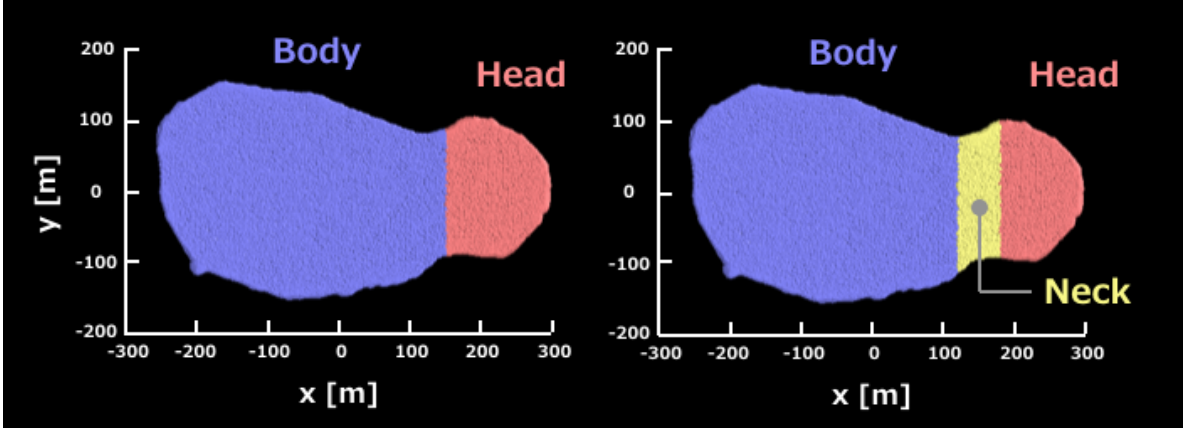


Figure 5: Density distributions considered for Itokawa. (Left) The densities of the body and head are treated as being different. (Right) The densities of the body, neck and head are treated as being different. This image represents a cross-section of the global shape model along the x-y plane viewed from the +z axis. The origin corresponds to the center-of-figure of the shape model.

of Figure 5. For this model, we consider the densities of the head and body to be the same, and the densities of the lobes and the neck are constrained by the total mass of the asteroid.

- The compressed neck with different density head and body model: This model differs from the previous one in that we allow the densities of the head, body and neck to vary. In practice, we pick the densities of two of the components and then solve for the third using the known total mass.

In the above models, we make use of the total mass of Itokawa  $3.58 \times 10^{10}$  kg, which was estimated by the Hayabusa GM measurement (Abe et al., 2006b). The shape model used in this study has a volume of  $1.77 \times 10^7$  m<sup>3</sup>, which corresponds to a mean bulk density of 2,020 kg/m<sup>3</sup>. This value is consistent with the bulk density of  $1,950 \pm 140$  kg/m<sup>3</sup> estimated by Abe et al. (2006b).

## 4. Results

For our first inversion, we made use of a simple model where the density of the head portion of Itokawa is different from the body part. We varied the densities of the two lobes and calculated the standard deviations of the dynamic elevations in each of the three region; MUSES-C, Sagamihara and Uchinoura. Given a specific density of the head, the density of the remaining body is uniquely determined using the total mass constraint. Figure 6 shows the standard deviations of the smooth terrain elevations as a function of the density of the head of Itokawa. The elevation standard deviations in all three extracted regions are minimized when the head of Itokawa has a higher density than the mean density  $2,020 \text{ kg/m}^3$ .

The blue solid line shows the results for the MUSES-C Regio including only the region 1-a to 1-c, whereas the combination of all five regions from 1-a to 1-e is shown with the blue dashed line. Of all investigated regions, the MUSES-C region is the most sensitive to variations in the density distribution, in part because this region is located closer to the mass concentration in the head than the other extracted regions. The elevation standard deviations for the Sagamihara and Uchinoura regions similarly indicated a mass concentration in the head. However, the flatness of the misfit curves shows that these two regions are less sensitive to the density variation in the x-axis direction. For example, whereas the standard deviation for MUSES-C varies from about 2 to 4 meters over the range of investigated values, the misfit for these two regions only varies by less than 0.5 meters. Finally, the black solid line combines all three regions together, which is a weighted average of the misfit values by the area of each region. This shows that the best fitting density of the head is  $2,450 \text{ kg/m}^3$ , and the corresponding density of the body is  $1,930 \text{ kg/m}^3$ . This best fitting model corresponds to a center-of-mass/center-of-figure offset of 9.9 meters in the direction of the head.

For our second model, we considered the case where there is a compressed neck between the two lobes of the head and body located between  $x = 120$  to  $180 \text{ m}$ . For this model, we here consider the case where the two lobes have the same density. Figure 7 shows misfit curves using data for the same smooth terrains as investigated in Figure 4 as a function of the density of the neck. The best fitting result for each of the three regions implies that the density of the

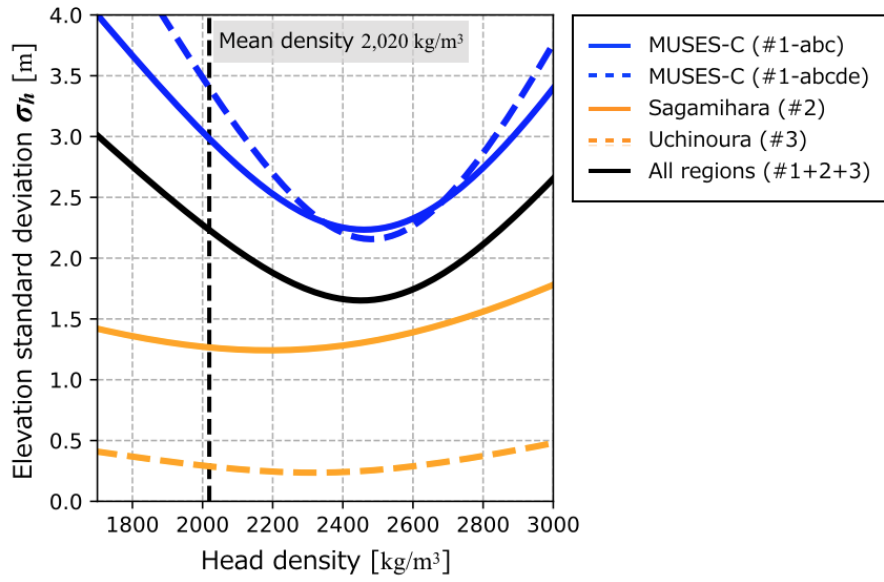


Figure 6: Standard deviations of the smooth terrain elevations as a function of the density of the head. The vertical line at  $2,020 \text{ kg/m}^3$  corresponds to the mean density of Itokawa. For the best fitting model that combines the three smooth regions (black solid line), the densities of the head and body are  $2,450 \text{ kg/m}^3$  and  $1,930 \text{ kg/m}^3$ , respectively.

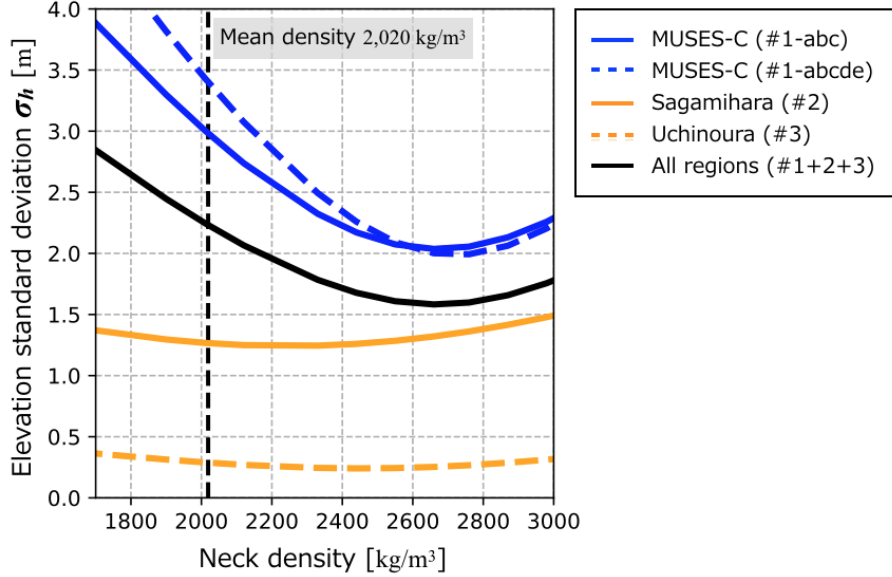


Figure 7: Standard deviations of the smooth terrain elevations as a function of the density of the neck. The vertical line at  $2,020 \text{ kg/m}^3$  corresponds to the bulk density of Itokawa. We here define the neck region of Itokawa as being located between  $x = 120$  and  $x = 180$  in the asteroid body-fixed frame. For the best fitting model that combines MUSES-C, Sagamihara and Uchinoura (black solid line), the density of the neck is  $2,660 \text{ kg/m}^3$  in contrast to a lower density of  $1,960 \text{ kg/m}^3$  for the remaining two lobes, the head and body.

neck is larger than the density of the two lobes.

Analogous to the simulations in Figure 6, the misfit is considerably more sensitive for the MUSES-C region than for the other two regions. This is simply because the mass concentration of the neck is closest to the MUSES-C, which is itself adjacent to the small head. The best fitting model that considers all three regions combined has a neck density of  $2,660 \text{ kg/m}^3$ , whereas the density of the two lobes is  $1,960 \text{ kg/m}^3$ . We note that the minimum misfit for this mass distribution model is comparable to, but slightly smaller than the previous model that considered only variations in density between the head and body. Based solely on model fitting, the compressed neck model should be favored over the model that considered only different densities for the head and body.

Finally, we consider the case where the densities of the head, neck and body all vary. For

324 these simulations, the density of the neck and head were first chosen, and then the density of the  
 325 body was computed using the total mass. As there are three parameters that are being varied,  
 326 we present our results which combine all three smooth terrains together, using 2-dimensional  
 327 misfit plots in the upper two panels of Figure 8. One plots shows the misfit  $\sigma_h$  as a function of  
 328 neck and head density (upper left), whereas the second shows the misfit as a function of the  
 329 body and head density (upper right). For these simulations, we used minimum and maximum  
 330 densities for each region that lie between 1,300 and 3,200 kg/m<sup>3</sup>, which corresponds to  
 331 approximately 60% and 0% porosity, respectively. The lower two panels of Figure 8 show  
 332 the center-of-mass/center-of-figure offset of Itokawa in the x-axis direction, using the same  
 333 densities as the upper panels. The white crosses denote a uniform density for every part of  
 334 Itokawa, whereas the magenta dots represent the best fitting density in this density structure  
 335 model. The centre-of-mass/center-of-figure offsets of 21 and 9 meters correspond to the best  
 336 fit and 1- $\sigma$  lower limit independently estimated by Lowry et al. (2014), respectively (see  
 337 discussion in Section 5).

338 These models show that the minimum misfit is obtained when the density of the neck is  
 339 higher than the average density of Itokawa. The neck density, however, trades off strongly with  
 340 the densities of the head and body, but the best fitting value (given our range of investigated  
 341 densities) is 3,200 kg/m<sup>3</sup>. For this value, the density of the head and body are respectively  
 342 1,400 and 2,000 kg/m<sup>3</sup>. For this model, the minimum misfit is equal to 1.53 m, which is lower  
 343 than the previous models that considered two variable densities.

344 The uncertainties of our density estimates are difficult to quantify as the density distribution  
 345 within Itokawa was assumed *a priori*. The defining boundaries of the head, neck and body are  
 346 subjective, and different choices would give rise to different inversion results. Nevertheless,  
 347 a few sources of systematic uncertainty can be assessed. First, the residuals of the shape  
 348 model estimation is likely to be 0.2 meters (Yoshikawa et al., 2012). Second, as a result of our  
 349 mascon approach for calculating the dynamical heights, these elevations could be uncertain  
 350 by a maximum of about 1 m, but on average less than 0.17 m in the smooth terrains. Lastly,  
 351 the smooth terrains are not completely smooth, and do contain isolated boulders that are not

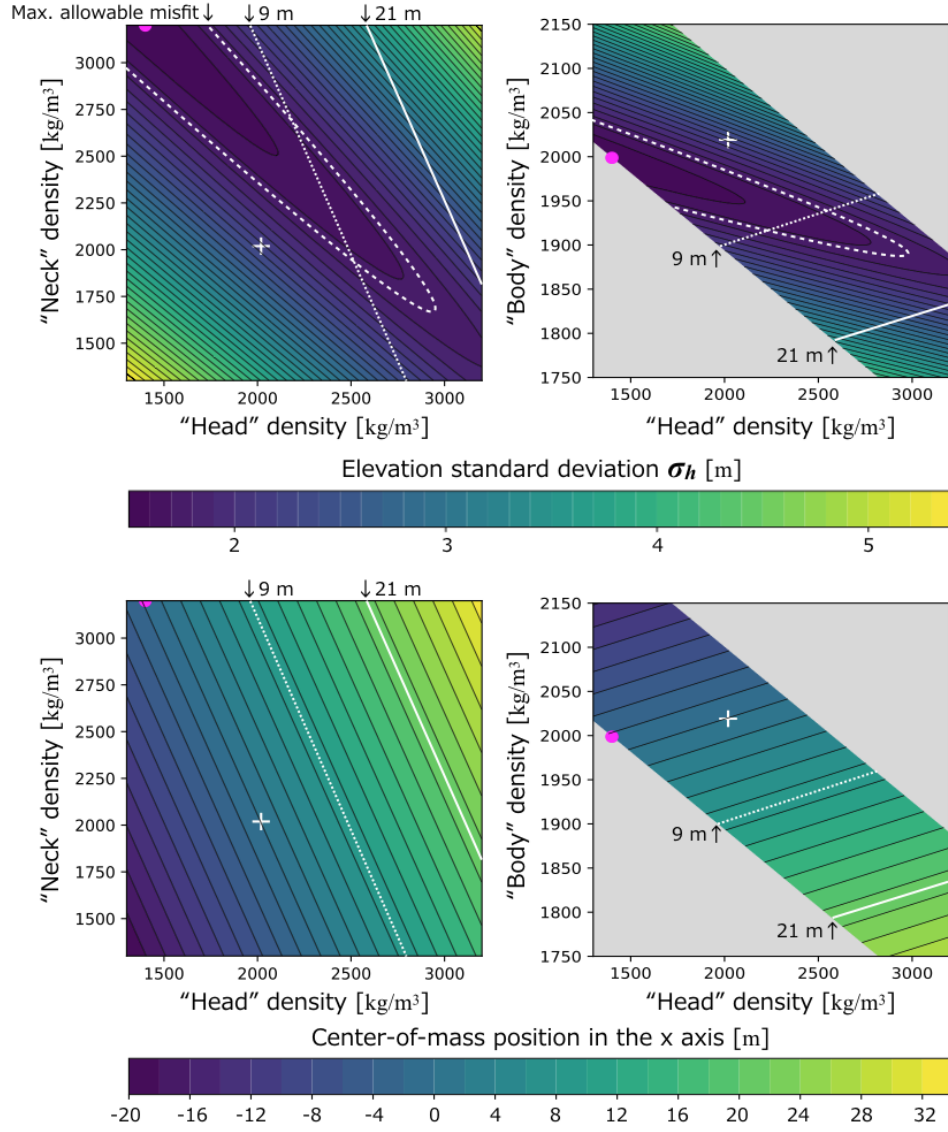


Figure 8: (top) Two-dimensional misfit plots for the density model where we allow the densities of three parts of Itokawa to vary. The color contours represent the standard deviations of the dynamic elevations in meters, which combines the three smooth terrains together, as a function of the densities of the neck and head (upper left) and the densities of the body and head (upper right). Grey regions in the right panel correspond to values that are unallowable given the total mass of the asteroid. White crosses represent a uniform density for all three parts. In this structure model, the best fitting densities of the head, neck and body are 1,400, 3,200 and 2,000 kg/m<sup>3</sup>, respectively (magenta dots). The lower two panels show the corresponding center-of-mass/center-of-figure offset in the x direction.



352 easily neglected. Based on our roughness calculations in Table 2, the smooth terrains typically  
353 have an intrinsic variability less than 0.15 m over 6 meter scales (excluding the small region  
354 1-c).

355 Based on the above considerations, we will estimate the uncertainty on the inversion  
356 parameters by allowing misfits that are 0.2 meters greater than the minimum value (white  
357 dashed curves in Figure 8). For our inversion that considered separate densities for the head,  
358 neck and body, we obtain the following ranges of acceptable densities for each region. For the  
359 neck region, densities are constrained to lie between, the maximum value of 3,200 and 1,690  
360  $\text{kg/m}^3$ . For the body, densities are tightly constrained to lie between 1,890 and 2,040  $\text{kg/m}^3$ .  
361 The head density is less constrained and can lie anywhere between the minimum value of  
362 1,300 and about 2,940  $\text{kg/m}^3$ . Finally, we note that the center-of-mass/center-of-figure offset  
363 can vary from -5 to 15 meters. Given a density structure model with fewer free parameters,  
364 we can more tightly constrain the density of each region. In the compressed head model, we  
365 obtained the best fitting density of 2,450  $\text{kg/m}^3$  for the head with an allowable range from  
366 2,220 to 2670  $\text{kg/m}^3$ , which are significantly higher than the density for the remaining body  
367 part. In the compressed neck model, the allowable range of the neck density is estimated to  
368 vary from 2,440 to 2,980  $\text{kg/m}^3$ . The inversion results for each density structure model are  
369 summarized in Table 3.

Table 3: Best fitting density in each structure model, the residual misfit of the dynamic elevations and the corresponding center-of-mass/center-of-figure offset (the second to fourth rows). The first row represents a uniform density for all regions of Itokawa. The bottom two rows show density distributions based on the COM-COF offset estimated by Lowry et al. (2014) using  $\Delta x = 21 \pm 12$  m. The density ranges in parentheses represents the estimated 1-sigma limits.

Density model	Best fitting density [kg/m <sup>3</sup> ]		Minimum misfit [m]		COM-COF offset [m]
	Head	Neck	Body	$\sigma_h$	
Uniform density	2,020	2,020	2,020	2.23	0.1
Compressed head	2,450 (2,220–2,670)	—	1,930 (1,880–1,980)	1.65 (1.65–1.85)	9.9 (4.7–15.0)
Compressed neck	1,960 (1,930–1,980)	2,660 (2,440–2,980)	1,960 (1,930–1,980)	1.58 (1.58–1.78)	4.5 (3.0–6.7)
Three parts vary	1,400 (1,300–2,940)	3,200 (1,690–3,200)	2,000 (1,890–2,040)	1.53 (1.53–1.73)	−1.6 (−5.4–15.2)
Compressed head	2,930 (2,410–3,460)	—	1,820 (1,710–1,930)	—	21 (9–33)
(Lowry et al., 2014)					
Compressed neck	1,740 (1,570–1,890)	5,070 (3,320–6,810)	1,740 (1,570–1,890)	—	21 (9–33)
(Lowry et al., 2014)					

## 5. Discussion

### 5.1. Density, porosity and formation mechanisms

Our inversions that consider only two regions with different densities show that Itokawa has a higher density in either the head or neck region than the average bulk density of the asteroid. For the inversion where the densities of the head and body were varied, the best fitting density of the head was found to be about 2,450 kg/m<sup>3</sup>, which is 27% larger than the body. For the inversion where the density of the neck was varied, the best fitting density was found to be about 2,660 kg/m<sup>3</sup>, which is 36% larger than the rest of the body. In both cases, the bulk density of the main body was found to be not too different than the average value of the asteroid as the head and neck regions are volumetrically small. Such a density inhomogeneity displaces the center-of-mass (COM) of Itokawa from the center-of-figure (COF) by about 3 to 15 meters (see Table 3).

The visible and near-infrared spectra acquired for Itokawa suggests that the composition of the surface is everywhere the same, and this composition is consistent with being composed of LL-chondritic materials that have a grain density of 3,190 kg/m<sup>3</sup> (Abe et al., 2006a). The variations in density that we find in our study are thus most easily explained by variations in porosity of a uniform composition asteroid. In the simple density structure model where the head and body have different densities, our best fitting densities of the two lobes correspond to bulk porosities of approximately 23% for the head and about 39% for the body. These porosities are representative of a coherent asteroid for the head and a rubble-pile structure for the body, respectively (Wilkison et al., 2002). The head of Itokawa thus may have a more coherent and monolithic structure than the body. As evidence for this, an area of steep slope of approximately 40 degrees is located near the head and neck, and is considered to be bedrock that is exposed on the surface (Barnouin-Jha et al., 2008).

For our model that allows all three regions to vary in density, the neck density is always found to be considerably greater than the head and body. For our assumed geometry of the neck, the density of the neck is constrained to lie between 3,200 and 1,690 kg/m<sup>3</sup>, which corresponds to 0% to 47% porosity. This model allows a large range of possible solutions, and

398 will be interpreted separately in the following section that employs additional independent  
399 constraints on the COM-COF offset of Itokawa.

400 There are several possible interpretations of our inversion results that bear on the origin  
401 and evolution of asteroid Itokawa. One model that fits the data has equal densities for the  
402 head and body, and a compressed density of the neck. This scenario would be consistent with  
403 both the head and body having formed from the same materials and with the same initial bulk  
404 porosities. The higher density of the neck region in this model is simply the result of the  
405 two bodies colliding and compacting the material at the interface between the two lobes. The  
406 impact of porous asteroids has been modeled by Davison et al. (2010). Though they do not  
407 report the final porosities of their simulations, they did find that significant heating can occur  
408 at the impact point as a result of the compaction of porosity. This compaction related heating  
409 was limited to a small region comparable in size to the neck in our models. In contrast, impact  
410 simulations by Jutzi and Benz (2016) that involve disruption and subsequent accumulation  
411 into a bi-lobed object with a low relative velocity predict that the porosity should decrease  
412 with depth within each pre-impact lobe. The connecting neck in their model would have a  
413 slightly lower density (and higher porosity) than the average value, which is inconsistent with  
414 our findings.

415 A second model that fits the data equally well is the case where the small head has a higher  
416 density (and lower porosity) than the body. Such a situation could arise in two ways. One  
417 possibility is that the head is simply a coherent block of material initially derived from a larger  
418 parent body, and that the body is a rubble pile asteroid formed by catastrophic disruption and  
419 re-accumulation. In this scenario, the head would represent a more pristine object that has  
420 undergone less processing by impacts and that later accreted to the main body. Alternatively,  
421 it is possible that the impact of the body and head compacted the porosity out of both the  
422 head and neck region. Given that the body is considerably larger in size, its initial porosity  
423 far from the impact point would have been relatively unaffected by the impact.

424 Asteroid 1999 KW4 is an interesting target for understanding dynamics of a binary system,  
425 which may be applicable to interpreting our results for Itokawa. This object is a binary system,

where the main body has a size of 1.32 km and the satellite has a smaller size of 0.45 km. From constraints on the orbital motion and shape modeling of each components based on ground-based radar observations by Ostro et al. (2006), the density of the primary is constrained to be about 1,970 (1,730–2,210) kg/m<sup>3</sup>, whereas the density of the satellite is found to have a higher density of 2,810 (2,180–3,630) kg/m<sup>3</sup>. The density difference between the two lobes of Itokawa inferred in this study can be explained by an eventual collapse of a binary system similar to that of 1999 KW4 (Scheeres et al., 2007). It remains to be seen if the density of the satellite of other binary systems is larger than the density of the primary object.

## 5.2. Comparison with YORP spin-up observations

The detection of a YORP spin-up/down of an asteroid can be used to model the large-scale density distribution in the body. The YORP effect is the change of the rotation rate of an irregularly shaped body that results from the torques related to the solar radiation and thermal emission (Rubincam, 2000), and the magnitude of this effect is sensitive to the COM-COF offset of the body (Scheeres and Gaskell, 2008). Based on the current shape model and rotation pole, a simulation of the YORP effect predicts that the rotation rate of Itokawa should be decelerating (Scheeres et al., 2007). However, Lowry et al. (2014) detected an acceleration of Itokawa’s rotation and estimated the COM-COF offset to be  $\Delta r = 14 \pm 7$  m in the x-y plane or  $\Delta x = 21 \pm 12$  m if the offset is assumed to be in the direction of the x axis. Given the symmetrical density structures investigated in our study, the COM-COF offset in the direction of the y axis for our models is always less than 0.5 meters for an arbitrary density distribution. Therefore, we will consider only the  $\Delta x$  offset as reported by Lowry et al. (2014).

To explain the observed YORP spin-up, Lowry et al. (2014) proposed two types of density distributions in Itokawa. Their models are similar to ours where the density of the head is higher than that for the body, or where there exists a compressed neck region. Using their  $\Delta x$  estimate along with our shape model, the COM-COF offset of  $21 \pm 12$  m corresponds to a density of 2,930 (2,410 to 3,460) kg/m<sup>3</sup> for the head and 1,820 (1,930 to 1,710) kg/m<sup>3</sup> for the body (see Table 3). Our best fitting densities and our predicted COM-COF offset of 9.9 m in the compressed head model is within the uncertainty of their estimation. Our model

where the density of the neck differs from the rest of the asteroid is less consistent with the COM-COF offset of Lowry et al. (2014). In particular, our best fitting model gives an offset of only 4.5 m, with a 1-sigma upper limit of 6.7 m, which is only marginally consistent with the 1-sigma lower limit of  $\Delta x = 9$  m from Lowry et al. (2014).

We next use the COM-COF offset of Lowry et al. (2014) to constrain our inversion that considered separate densities for the head, neck and body. We noted previously that this inversion provided a wide range of possibilities as a result of trade-offs between the three densities. As previously discussed, Figure 8 plots our misfit as a function of the density of the three components. The white dashed curve gives our estimate of the 1-sigma uncertainty, showing that there is a strong correlation between the density of the head and neck. In this same plot, we plot solid and dotted white lines corresponding the best fit and 1-sigma lower limit of the Lowry et al. (2014) COM-COF offset. This shows that there is only a small region of the parameter space that overlaps at the 1-sigma level. In particular, the two techniques constrain the density of the head to lie between 2,200 and 2,940 kg/m<sup>3</sup>, which is always greater than the average density of the asteroid. The density of the neck is constrained to lie between 1,690 and 2,650 kg/m<sup>3</sup>, allowing for either moderate compaction of the neck region, or even a moderate increase in porosity. The density of the body is well constrained between the limits of 1,890 and 1,940 kg/m<sup>3</sup>, which is slightly lower than the mean bulk density of 2,020 kg/m<sup>3</sup> in this study. Thus, the best constrained result using both techniques is that the head of Itokawa has a higher density than the rest of the asteroid.

## 6. Conclusion

This study developed a technique to estimate the interior density distribution within the asteroid Itokawa based on the elevations of the smooth terrains with respect to an equipotential surface. By changing the interior density distribution, we searched for solutions that made these surfaces as flat as possible. This study indicates that Itokawa has an important density heterogeneity between the two lobes, where the head is found to have a higher density than the body. Models with a compressed neck can also fit the data, but are not required when

481 considering the independent COM-COF offset inferred from the observed YORP spin-up of  
482 the asteroid by Lowry et al. (2014). Our results imply that the head has a lower porosity than  
483 the remainder of the body (23% vs. 39%). This could arise either if the head is composed of a  
484 coherent block of material derived from a larger parent body, or if a portion of the porosity of  
485 the head was compacted out when the head and body collided to form the presently observed  
486 asteroid.

487 Our technique of using smooth terrains to constrain the density distribution in a small  
488 body can be applied to investigate any arbitrary density distribution such as the presence of a  
489 central core-like structure with a lower porosity at the center of an asteroid. Additionally, this  
490 technique can be applied to any irregularly shaped small body which possesses a flat region  
491 that could be approximated as the equi-potential surface. Possible small bodies that could  
492 be investigated include Comet 103P/Hartley 2 and Comet 67P/Churyumov-Gerasimenko, as  
493 well as Ultima Thule (the Kuiper Belt object officially named 2014 MU69). Our estimation  
494 technique will be a useful for constraining the effects of collisions in the asteroid belt and can  
495 be used as constraints for impact simulations of porous planetesimals. Improved modeling of  
496 collisions in the asteroid belt are required to better understand how the collisions affect the  
497 porosities of the bodies.

## Acknowledgement

This study was supported by Japan Society for the Promotion of Science (JSPS) Core-to-Core Program, "International Network of Planetary Sciences". M.K. acknowledges support from Cross-Boundary Innovation Program in Osaka University. Numerical simulations were in part carried out on PC clusters and computers at Center for Computational Astrophysics, National Astronomical Observatory of Japan. This study is also supported by JSPS KAKENHI No. 18H01267. M.W. was supported by the French Space Agency, CNES.

## References

Abe, M, Y Takagi, K Kitazato, S Abe, T Hiroi, F Vilas, B E Clark, P A Abell, S M

- Lederer, K S Jarvis, T Nimura, Y Ueda, and A Fujiwara**, “Near-Infrared Spectral Results of Asteroid Itokawa from the Hayabusa Spacecraft,” *Science*, 2006, *312* (5778), 1334–1338.
- Abe, Shinsuke, Tadashi Mukai, Naru Hirata, Olivier S Barnouin-Jha, Andrew F Cheng, Hirohide Demura, Robert W Gaskell, Tatsuaki Hashimoto, Kensuke Hiraoka, Takayuki Honda, Takashi Kubota, Masatoshi Matsuoka, Takahide Mizuno, Ryosuke Nakamura, Daniel J Scheeres, and Makoto Yoshikawa**, “Mass and Local Topography Measurements of Itokawa by Hayabusa,” *Science*, 2006, *312* (5778), 1344–1347.
- Barnouin-Jha, Olivier S., Andrew F. Cheng, Tadashi Mukai, Shinsuke Abe, Naru Hirata, Ryosuke Nakamura, Robert W. Gaskell, Jun Saito, and Beth E. Clark**, “Small-scale topography of 25143 Itokawa from the Hayabusa laser altimeter,” *Icarus*, 2008, *198* (1), 108–124.
- Carry, B.**, “Density of asteroids,” *Planetary and Space Science*, 2012, *73* (1), 98–118.
- Davison, T. M., G. S. Collins, and F. J. Ciesla**, “Numerical modelling of heating in porous planetesimal collisions,” *Icarus*, 2010, *208* (1), 468–481.
- Demura, Hirohide, Shingo Kobayashi, Etsuko Nemoto, Naoya Matsumoto, Motohiro Furuya, Akira Yukishita, Noboru Muranaka, Hideo Morita, Ken Shirakawa, Makoto Maruya, Hiroshi Ohyama, Masashi Uo, Takashi Kubota, Tatsuaki Hashimoto, Jun\textquoterightchiro Kawaguchi, Akira Fujiwara, Jun Saito, Sho Sasaki, Hideaki Miyamoto, and Naru Hirata**, “Pole and Global Shape of 25143 Itokawa,” *Science*, 2006, *312* (5778), 1347–1349.
- Ernst, C. M., O. S. Barnouin, R. T. Daly, and the Small Body Mapping Tool Team**, “The Small Body Mapping Tool (SBMT) For Accessing, Visualising, and Analyzing Spacecraft Data in Three Dimensions,” in “49th Lunar and Planetary Science Conference 2018” 2018.



**Fujiwara, A, J Kawaguchi, D K Yeomans, M Abe, T Mukai, T Okada, J Saito, H Yano, M Yoshikawa, D J Scheeres, O Barnouin-Jha, A F Cheng, H Demura, R W Gaskell, N Hirata, H Ikeda, T Kominato, H Miyamoto, A M Nakamura, R Nakamura, S Sasaki, and K Uesugi**, “The Rubble-Pile Asteroid Itokawa as Observed by Hayabusa,” *Science*, 2006, *312* (5778), 1330–1334.

**Hirata, Naru, Olivier S. Barnouin-Jha, Chikatoshi Honda, Ryosuke Nakamura, Hideaki Miyamoto, Sho Sasaki, Hirohide Demura, Akiko M. Nakamura, Tatsuhiro Michikami, Robert W. Gaskell, and Jun Saito**, “A survey of possible impact structures on 25143 Itokawa,” *Icarus*, 2009, *200* (2), 486–502.

**Hirt, Christian and Michael Kuhn**, “Convergence and divergence in spherical harmonic series of the gravitational field generated by high-resolution planetary topography: A case study for the Moon,” *Journal of Geophysical Research: Planets*, 2017, *122* (8), 1727–1746.

**Jutzi, M. and W. Benz**, “Formation of bi-lobed shapes by sub-catastrophic collisions: A late origin of comet 67P/C-G’s structure,” *Astronomy and Astrophysics*, jan 2016, *597*, A62.

**KANAMARU, Masanori and Sho SASAKI**, “Estimation of Interior Density Distribution for Small Bodies: The Case of Asteroid Itokawa,” *Transactions of the Japan Society for Aeronautical and Space Sciences, Aerospace Technology Japan*, 2019, *advpub*.

**Konopliv, Alexander S., James K. Miller, William M. Owen, Donald K. Yeomans, Jon D. Giorgini, Romain Garmier, and Jean Pierre Barriot**, “A global solution for the gravity field, rotation, landmarks, and ephemeris of Eros,” *Icarus*, 2002, *160* (2), 289–299.

**Lowry, S. C., P. R. Weissman, S. R. Duddy, B. Rozitis, A. Fitzsimmons, S. F. Green, M. D. Hicks, C. Snodgrass, S. D. Wolters, S. R. Chesley, J. Pittichová, and P. van Oers**, “The internal structure of asteroid (25143) Itokawa as revealed by detection of YORP spin-up,” *Astronomy and Astrophysics*, 2014, *562*, A48.

- Miller, J. K., A. S. Konopliv, P. G. Antreasian, J. J. Bordi, S. Chesley, C. E. Helfrich, W. M. Owen, T. C. Wang, B. G. Williams, D. K. Yeomans, and D. J. Scheeres**, “Determination of shape, gravity, and rotational state of asteroid 433 Eros,” *Icarus*, 2002, *155* (1), 3–17.
- Miyamoto, Hideaki, Hajime Yano, Daniel J Scheeres, Shinsuke Abe, Olivier Barnouin-Jha, Andrew F Cheng, Hirohide Demura, Robert W Gaskell, Naru Hirata, Masateru Ishiguro, Tatsuhiro Michikami, Akiko M Nakamura, Ryosuke Nakamura, Jun Saito, and Sho Sasaki**, “Regolith Migration and Sorting on Asteroid Itokawa,” *Science*, 2007, *316* (5827), 1011–1014.
- Motooka, Norizumi and Jun’ichiro Kawaguchi**, “Study on the gravity field on the surface of Itokawa,” in “the 22nd Workshop on JAXA Astrodynamics and Flight Mechanics” 2012, pp. A–15.
- Nakamura, Tsuko, Akiko M Nakamura, Jun Saito, Sho Sasaki, Ryosuke Nakamura, Hirohide Demura, Hiroaki Akiyama, David Tholen, and AMICA team**, “Multi-band imaging camera and its sciences for the Japanese near-earth asteroid mission MUSES-C,” *Earth, Planets and Space*, nov 2001, *53* (11), 1047–1063.
- Neumann, Wladimir, Doris Breuer, and Tilman Spohn**, “The thermo-chemical evolution of Asteroid 21 Lutetia,” *Icarus*, 2013, *224* (1), 126–143.
- Ostro, Steven. J., J.-L. Margot, L. A. M. Benner, J. D. Giorgini, D. J. Scheeres, E. G. Fahnestock, S. B. Broschart, J. Bellerose, M. C. Nolan, C. Magri, P. Pravec, P. Scheirich, R. Rose, R. F. Jurgens, E. M. De Jong, and S. Suzuki**, “Radar Imaging of Binary Near-Earth Asteroid (66391) 1999 KW4,” *Science*, 2006, *314* (5803), 1276–1280.
- Ramachandran, P and G Varoquaux**, “Mayavi: 3D Visualization of Scientific Data,” *Computing in Science & Engineering*, 2011, *13* (2), 40–51.

- Richardson, James E and Timothy J Bowling**, “Investigating the combined effects of shape, density, and rotation on small body surface slopes and erosion rates,” *Icarus*, 2014, 234, 53–65.
- Rubincam, David Parry**, “Radiative Spin-up and Spin-down of Small Asteroids,” *Icarus*, 2000, 148 (1), 2–11.
- Saito, J, H Miyamoto, R Nakamura, M Ishiguro, T Michikami, A M Nakamura, H Demura, S Sasaki, N Hirata, C Honda, A Yamamoto, Y Yokota, T Fuse, F Yoshida, D J Tholen, R W Gaskell, T Hashimoto, T Kubota, Y Higuchi, T Nakamura, P Smith, K Hiraoka, T Honda, S Kobayashi, M Furuya, N Matsumoto, E Nemoto, A Yukishita, K Kitazato, B Dermawan, A Sogame, J Terazono, C Shinohara, and H Akiyama**, “Detailed Images of Asteroid 25143 Itokawa from Hayabusa,” *Science*, 2006, 312 (5778), 1341–1344.
- Scheeres, D J and R W Gaskell**, “Effect of density inhomogeneity on YORP: The case of Itokawa,” *Icarus*, 2008, 198 (1), 125–129.
- Scheeres, D. J., M. Abe, M. Yoshikawa, R. Nakamura, R. W. Gaskell, and P. A. Abell**, “The effect of YORP on Itokawa,” *Icarus*, 2007, 188 (2), 425–429.
- Scheeres, D.J, B Khushalani, and R.A Werner**, “Estimating asteroid density distributions from shape and gravity information,” *Planetary and Space Science*, 2002, 48 (10), 965–971.
- Schöberl, Joachim**, “An advancing front 2D/3D-mesh generator based on abstract rules,” *Computing and Visualization in Science*, jul 1997, 1 (1), 41–52.
- Stooke, P.**, “Stooke Small Bodies Maps MULTI-SA-MULTI-6-STOOKEMAPS-V2.0.,” 2012.
- Takahashi, Yu and D J Scheeres**, “Morphology driven density distribution estimation for small bodies,” *Icarus*, 2014, 233, 179–193.

- Thomas, P C**, “Gravity, Tides, and Topography on Small Satellites and Asteroids: Application to Surface Features of the Martian Satellites,” *Icarus*, 1993, 105 (2), 326–344.
- Veverka, J., M. Robinson, P. Thomas, S. Murchie, J. F. Bell, N. Izenberg, C. Chapman, A. Harch, M. Bell, B. Carcich, A. Cheng, B. Clark, D. Domingue, D. Dunham, R. Farquhar, M. J. Gaffey, E. Hawkins, J. Joseph, R. Kirk, H. Li, P. Lucey, M. Malin, P. Martin, L. McFadden, W. J. Merline, J. K. Miller, Jr Owen, C. Peterson, L. Prockter, J. Warren, D. Wellnitz, B. G. Williams, and D. K. Yeomans**, “NEAR at Eros: Imaging and spectral results,” *Science*, 2000, 289 (5487), 2088–2097.
- Werner, R. A. and D. J. Scheeres**, “Exterior Gravitation of a Polyhedron Derived and Compared with Harmonic and Mascon Gravitation Representations of Asteroid 4769 Castalia,” *Celestial Mechanics and Dynamical Astronomy*, 1997, 65, 313–344.
- Werner, Robert A**, “Spherical harmonic coefficients for the potential of a constant-density polyhedron,” *Computers & Geosciences*, 1997, 23 (10), 1071–1077.
- Wilkison, Sarah L., Mark S. Robinson, Peter C. Thomas, Joseph Veverka, Timothy J. McCoy, Scott L. Murchie, Louise M. Prockter, and Donald K. Yeomans**, “An estimate of Eros’s porosity and implications for internal structure,” *Icarus*, 2002, 155 (1), 94–103.
- Yeomans, D K, P G Antreasian, J.-P. Barriot, S R Chesley, D W Dunham, R W Farquhar, J D Giorgini, C E Helfrich, A S Konopliv, J V McAdams, J K Miller, W M Owen, D J Scheeres, P C Thomas, J Veverka, and B G Williams**, “Radio Science Results During the NEAR-Shoemaker Spacecraft Rendezvous with Eros,” *Science*, 2000, 289 (5487), 2085–2088.
- Yoshikawa, M., J. Kawaguchi, Naru Hirata, T. Kubota, T. Mukai, Olivier Barnouin-Jha, T. Kominato, K. Shirakawa, Daniel Scheeres, Robert Gaskell, M. Ishiguro, T. Hashimoto, Shinsuke Abe, and Jun Saito**, “Landmark Navigation Studies and Target Characterization in the Hayabusa Encounter with Itokawa,” in “AIAA/AAS Astrodynam-

ics Specialist Conference and Exhibit” Guidance, Navigation, and Control and Co-located Conferences, American Institute of Aeronautics and Astronautics, aug 2012, p. 6660.